Int J Adv Manuf Technol (2009) 45:430–447
DOI 10.1007/s00170-009-1989-8

ORIGINAL ARTICLE

Chip formation analysis in micromilling operation

Jinsheng Wang · Yadong Gong · Gabriel Abba · Jean Francois Antoine · Jiashun Shi

Received: 11 September 2008 / Accepted: 18 February 2009 / Published online: 7 March 2009

Abstract In mechanical micromachining, understanding the chip formation mechanism is critical to optimize the machining parameters and improve the workpiece performance. In this work, the entire slot micromilling process on Al6061-T6 by one flute carbide cutter was simulated by means of finite element method (FEM). Under this machining parameters set, the chip was found to be segmented type. The simulation results matched with the experimental results on the burr and chip morphologies and the cutting force. The segmented chip formation process was described from the viewpoint of chip velocity. The variations of the tool chip contact length (l_T) and the shear band length (l_S) were studied in detail. The chip formation mechanism was studied quantitatively by means of hybrid analytical-FEM approach. Through calculating the chip moments, "tool rake moment" M_{Tool} and "shear band moment" M_{Work}, it has been found that the main reasons of the segmented chip formation are the variations of the l_T and l_S. The Arcona–Dow model (AD model) and Merchant model (MM model) were utilized to calculate the M_{Work} respectively. The AD model performed better in the microscale than the MM model. In the segment generation occasion, the average chip velocity value in chip bending process was much greater than the one before chip bending, which was about the cutting speed. The chip root velocity was almost constant in the entire micromilling process, and the chip tip velocity increased greatly in the chip bending instant due to the chip angular acceleration. The chip angular acceleration was acquired, respectively, from FEM and the analytical method based on the M_{Tool} and $M_{\text{Work\_AD}}$ calculations. The agreement of these two approaches validated the correctness of the chip moments calculations. The results of this work were useful to understand the micromilling mechanism and improve the workpiece performances.

Keywords Micromilling · FEM · Segmented chip formation · Chip moments · Chip velocity · Chip angular acceleration · Cutting force model

This work is financial supported by Chinese 985-II foundation, Northeastern University outstanding PhD project foundation (200705), French Research Ministry, and Lorraine Region Council.

J. Wang (✉) · Y. Gong · J. Shi
Laboratory of Advanced Manufacturing and Automation, Northeastern University, Shenyang, China
e-mail: jswang@neu.com.cn, Jinsheng.WANG-0@etudiants.ensam.fr

Y. Gong
e-mail: gongyd@mail.neu.edu.cn

J. Shi
e-mail: jshshi@mail.neu.edu.cn

J. Wang · G. Abba · J. F. Antoine
Laboratoire de Génie Industriel et de Production Mécanique, Université de Paul Verlaine, Metz, France

G. Abba
e-mail: abba@univ-metz.fr

J. F. Antoine
e-mail: Jean-Francois.ANTOINE@iutnb.uhp-nancy.fr

1 Introduction

Micromilling operation is an attractive way to fabricate the miniature components. It has been essentially recognized that the merits of the micromilling

include lower cost, flexibility, and material compatibility, not only on silicon as lithography [1]. It is an effective method to fabricate the complex microgeometric shapes for the applications of the microdies and molds, biomedical, and MEMS [2–5].

Lack of chip control often leads to the coarse machined surface, poor machining accuracy, and problems of chip removal from the machining zone [6]. In the micromilling process, because the residual burrs on the workpiece are not easily eliminated by the conventional burr removal processes, they degrade the quality of the micromilled components. Hence, in order to minimize the burr generation, the micromilling chip formation mechanism should be studied deeply. Ueda et al. [7] found the lamellar chip structure when microcutting an amorphous metal. They found the chip lamellar was induced by the periodical localization of the shear band. However, the tool edge radius effect was neglected in this research. Lee and Dornfeld [8] conducted many micromilling experiments to study the relationship between the burr formation and the machining variables in order to optimize the machining variables. Because too many experiments are time-consuming and expensive, meaningful simulations are helpful to study the chip formation process cost effectively.

With the enhancement of the digital computer industry, the finite element method (FEM) is widely used to understand the chip formation mechanism in the multiphysics scale [9–11]. In order to simulate the real micromachining condition, more computational resources and longer duration are required because of the finer element mesh and greater element number. Vogler et al. [12] used a customized FEM code developed by Chuzhoy et al. [13] to determine the minimum chip thicknesses (MCT) for ferrite and pearlite metallographies, respectively. Simoneau et al. [14] assigned different hardness parameters to different metal-phase components of steel and explained the chip formation and surface defects in microscale cutting. Dhanorker and Özel [15] predicted the chip formation and temperature fields for meso/microscale milling; they found the temperature of the micromilling process was lower compared to the one of conventional cutting. Woon et al. [16] discussed the relationship between the ratio of uncut chip thickness (UCT) to tool edge radius and the chip formation mechanism, material deformation, and stress distributions in the microcutting. Besides the FEM, molecular dynamics simulation is another way to study the machining process from the microscale to the nanoscale [17].

In this work, the finite element model of micromilling Al6061-T6 alloy by a carbide tool was established to study the chip formation mechanism. The chip was found to be the segmented type, which was verified by the experimental observation of burr and chip morphology. The average simulated cutting force matched the experimental force within 5% error. The variations of the chip velocity field, the tool chip contact length (l_T), and the shear band length (l_S) were focused in the segmented chip formation process. The chip formation mechanism was studied quantitatively by means of a hybrid analytical–FEM approach. By calculating the chip moments exactly, it has been found that the primary reasons for the segmented chip generation were the variations of l_T and l_S. The chip angular acceleration was calculated to validate the chip moment calculations.

2 FEM simulation

2.1 FEM model

In material removal processes using geometrically defined cutting edges, workpiece material undergoes severe deformation and shearing at very high deformation rates and, sometimes, high temperatures. Hence, adopting the reliable workpiece material flow stress data, also as well known as the constitutive model, which covers the large strain rate and temperature range, is important to characterize the material behavior in the vicinity of the cutting edge [18]. The friction between the tool and workpiece is as important as the material flow stress model [19]. In this paper, the constitutive and friction models were chosen based on the literatures according to the machining conditions in the micromilling process.

2.1.1 Tool and workpiece choices

About all commercial micromill tool materials are tungsten carbide, which has high hardness and strength at high temperatures. In this study, a two-flute tungsten carbide micromill was utilized.

Al6061-T6 alloy has excellent comprehensive performance, which is one of the most promising candidates for fabricating thermally stable, high-strength, and light-weight micro components. In the microcutting, Al6061-T6 has been selected as the experimental materials in many researches [8, 20, 21]. Meanwhile, because the properties of Al6061-T6 are similar to the most widely utilized aluminum materials, Al6061-T6 can be considered as their representative. Therefore, the analytical results of this study are useful for understanding the micromilling mechanism, even to other materials.

2.1.2 Material constitutive model

The flow stress at which the workpiece material starts to plastically deform is influenced by strain, strain rate, temperature factors, and sometimes strain paths. The Johnson–Cook (JC) model shown in Eq. 1 is widely accepted in machining simulation due to its good fit for strain-hardening and thermal softening behavior of metals and its numerical robustness, and it can be easily used in finite element simulation models. The constants for Al6061-T6 [22] are listed in Table 1.

$$\bar{\sigma} = [A + B(\bar{\varepsilon})^n][1 + C\ln(\frac{\dot{\bar{\varepsilon}}}{\dot{\varepsilon}_0})][1 - (\frac{T - T_{room}}{T_{melt} - T_{room}})^m] \quad (1)$$

$\bar{\sigma}$	Von Mises flow stress
$\bar{\varepsilon}$	equivalent plastic strain
$\dot{\bar{\varepsilon}}$	strain rate
$\frac{\dot{\bar{\varepsilon}}}{\dot{\varepsilon}_0}$	is the dimensionless plastic strain rate for $\dot{\varepsilon}_0 = 1.0\ \mathrm{s}^{-1}$
T	workpiece temperature
T_{room}	room temperature
T_{melt}	workpiece melt temperature
A	yield stress
B and n	effects of the strain hardening with B is hardening constant and n is hardening exponent
C	strain rate constant
m	thermal softening exponent

2.1.3 Friction model

The friction behavior in the cutting zone is still not clear, even if many works have been done on this topic [9, 23]. In the low cutting speed range, the friction stress τ_f on the tool rake face is assumed to be proportional to the normal stress σ_n, with a coefficient of friction, μ. This is the sliding friction based on the Coulomb's law as

$$\tau_f = \mu \cdot \sigma_n \quad (2)$$

According to Trent and Wright's work [24], the sliding friction was dominant during the low-speed machining. The sticking friction was dominant during the high-speed machining. In micromilling, even if a high-speed spindle is adopted to improve the cutting speed, the cutting speed remains much lower than the conventional one due to the tiny tool diameter. In this case, the cutting speed was 238.8 mm/s. Therefore, the Coulomb's law of sliding friction was dominant in the micromilling operation. In this work, for the combination of the tool and workpiece materials, carbide and Al6061-T6, the friction factor μ was chosen as 0.7, obtained from experiments by Medaska et al. [25].

Table 1 Al6061-T6 material constants in JC model

A(MPa)	B(MPa)	n	C	m	Others
324	114	0.42	0.002	1.34	$T_{\mathrm{melt}} = 582°\mathrm{C} = 855.15\mathrm{K}$ $T_{\mathrm{room}} = 20°\mathrm{C} = 293.15\mathrm{K}$

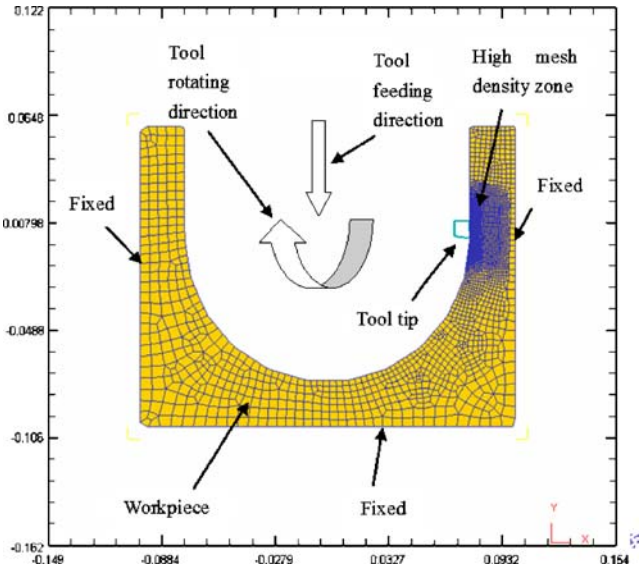

Fig. 1 FEM model

2.1.4 Simulation setup

In this study, DEFORM-2D from SFTC was used to simulate the cutting process. This package is based

Table 2 Simulation parameters

Tool geometry	
Tool diameter (μm)	152
Flutes no.	2
Edge radius (μm)	1.34
Rake angle (°)	6.5
Clearance angle (°)	5
Material properties of Al6061-T6	
Young's modulus (GPa)	68.9
Poisson ratio	0.33
Thermal conductivity (W/m − K)	167
Heat capacity (J/g −° C)	0.896
Machining parameters	
Rotating speed (RPM)	30000
Feed rate (mm/min)	10
Cutting depth (μm)	20
Room temperature (°C)	20

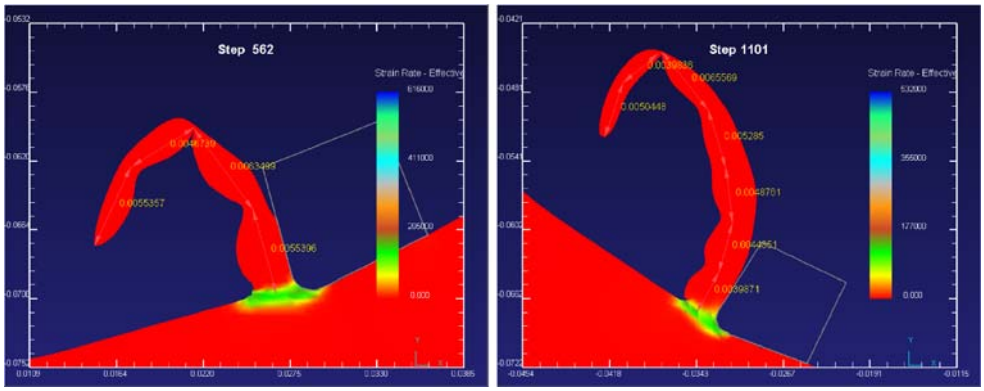

Fig. 2 Simulated segmented chip (**a**, **b**)

(a) After rotating 72.2° (b) After rotating 121°

on an updated Lagrangian formulation that employs the implicit integration method designed for large deformation simulations. The strength of DEFORM-2D is its ability to automatically remesh and generate a very dense grid of nodes near the tool tip so that large gradients of strain, strain rate, and temperature can be handled. Hence, no chip separation criterion is needed, which makes it highly effective in simulating the metal cutting process. Furthermore, a high mesh density zone is defined around the cutting edge as a moving window allowing an excessively distorted mesh in the primary and secondary shear zones to be automatically remeshed without interruption. Thus, the chip formation is simulated step by step in a minimum number of remeshings with per-tool advance.

In this simulation, due to the small cutting depth, the effect of the helix angle was neglected, and then the flute was assumed to be straight. Due to the small feed rate, cutting by the bottom edge was not included, and only the side edge was considered. Hence, the micromilling process was simplified as a plane strain problem and modeled by DEFORM-2D. The workpiece was treated as elastic–plastic type, and the tool was considered as a rigid body. In our simulation, the total element number of the meshed workpiece was 18,404. Supported by the mesh density window technique, the tool work contact region was highly meshed with the smallest element size reducing to 80 nm approximately, and the whole slot cutting process by one flute was simulated with 1,400 steps and 310 remeshes. Figure 1 showed the detail of this FEM model, with the boundary condition, mesh of the workpiece, and tool movement information.

The JC constitutive model was embedded into the simulation engine by the user routine, and the friction model was chosen as mentioned in Section 2.1.3. The other material thermal and mechanical properties for Al6061-T6 were obtained from www.matweb.com. The machining parameters were designed coincident with the experiment, and the feed rate was chosen very low in order to avoid the tool premature failure and to prevent the collapse of the 2D hypothesis. These parameters were listed in Table 2.

2.2 Simulation results

The simulated segmented chip morphology with four and seven segments in the micromilling process were

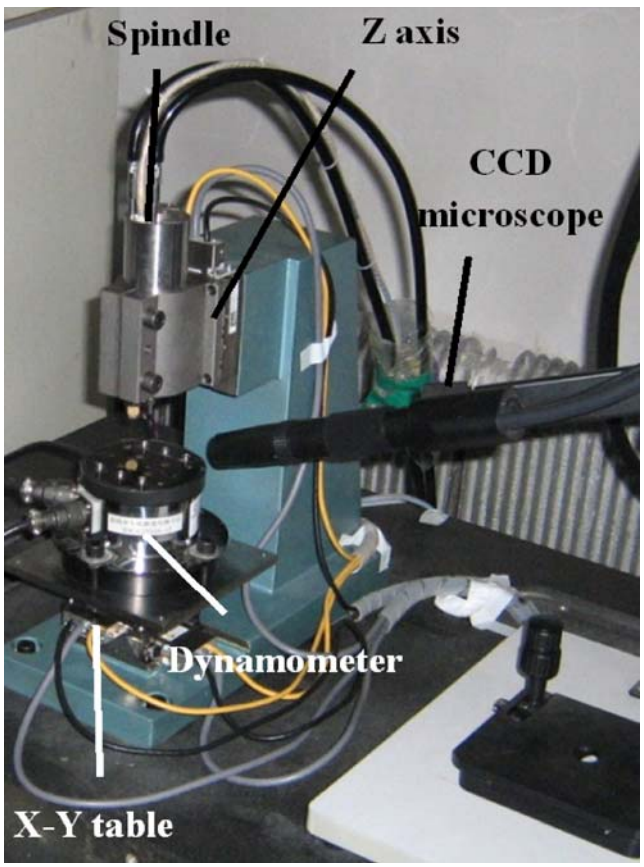

Fig. 3 Micro machine tool

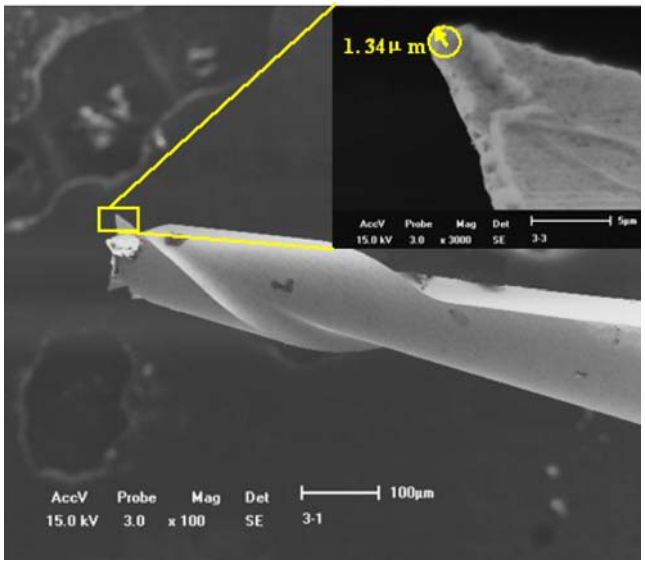

Fig. 4 Micromill and tool tip

(a) Top Burr

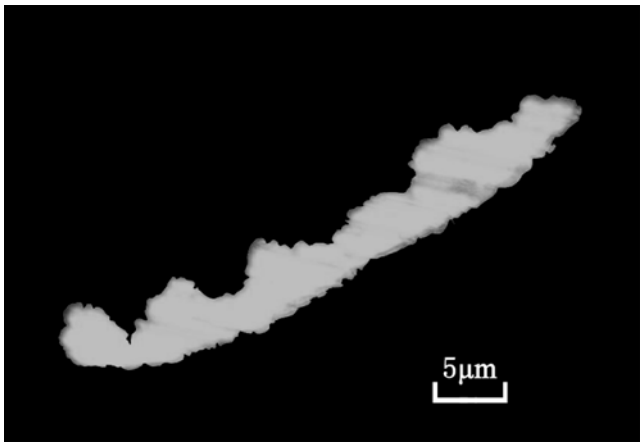

(b) Chip sample 1

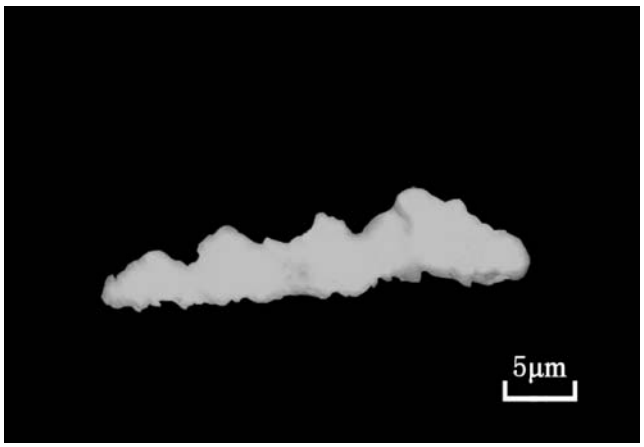

(c) Chip sample 2

Fig. 5 Experimental burr and chips (**a**–**c**)

shown in Fig. 2a and b, respectively. The length of each segment in millimeter units is labeled in the figure. The length of each segment on them was an approximate value because the segment shape depended on the mesh density. When the chip moved out of the mesh density window, it might have lost its real shape due to remesh. However, the newly formed segment with a finer element had an exact shape, and its length was measured just after it was generated. When the tooth exited the machined slot, the chip was composed of 11 segments. The average segment length was 4.7835 μm, with 0.6645 μm standard deviation.

3 Experimental validations

3.1 Experimental setup

In order to validate the simulated chip formation, the micromilling experiment was conducted on a 3D micro machine tool as shown in Fig. 3. Three linear motors with 10 nm resolution and 50 mm stroke were equipped to drive the motion of the X–Y table and the Z axis. An electro spindle with 60,000 rpm maximal speed was installed on the Z axis. A two-flute M.A.Ford tungsten carbide micromill with 152 μm diameter and 1.34 μm edge radius, as shown in Fig. 4, was chucked in the collet. A precision three-channel dynamometer with 10 mN threshold was placed on the X–Y table to record the experimental cutting forces. A charge-coupled de-

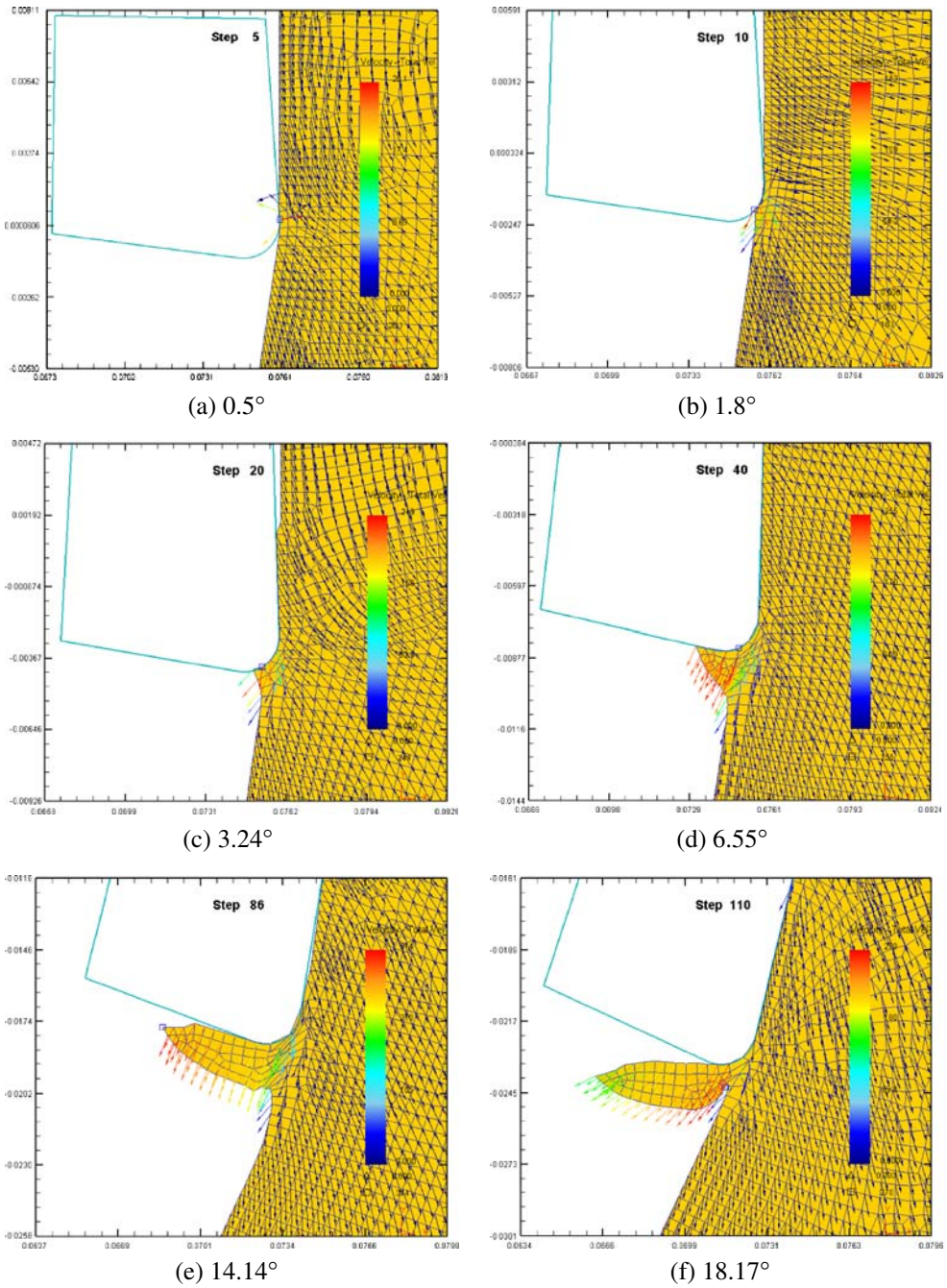

(a) 0.5° (b) 1.8° (c) 3.24° (d) 6.55° (e) 14.14° (f) 18.17°

Fig. 6 The first segment formation process (**a**–**f**)

vice microscope was used to monitor the micromilling process online. All the experimental parameters were listed in Table 2.

3.2 Experimental results

From the SEM photo of the top burr, as shown in Fig. 5a, there were many parallel segments distributed on the free surface. The microchips were collected and embedded in the resin, polished, and viewed under the optical microscope. Two chip examples were shown in Fig. 5b, c. The segment was observed, with 5.79 μm average segment length and 1.36 μm standard deviation. The chip morphology matched the simulation chip shape well.

The micromilling experimental force signals were recorded by the dynamometer. The peak-to-valley values of the experimental X and Y forces averaged over 50 revolutions were calculated and compared with the simulation cutting force. The experimental X and Y forces were 0.462 and 0.475 N. The corresponding simulation results were 0.446 and 0.453 N. The relative

errors were within 5%. Therefore, the simulation results were believed to be correct and capable of providing better understanding of the chip formation mechanism.

4 Chip formation process

The segmented chip has been found in the macroscale machining, especially when manufacturing hardened metals [26]. To the micromilling, the chip mass varies in the entire process, which is much smaller than the one in the conventional machining. Hence, the chip velocity would be apparently different to the segmented chip in the macroscale. In this section, the variation of chip velocity field in the micromilling process was described in detail.

4.1 Chip formation process with velocity variation

The first two segment formation processes were given in Figs. 6 and 7. The state variable of these series was the total node velocity obtained from the FEM.

At the beginning of tool workpiece engagement, the UCT was quite small. The ploughing effect was dominant in the tool work contact region. The tool edge pressed the workpiece, but the chip velocity magnitude was smaller due to the tool being moved in the tangential direction, Fig. 6a. As the tool advanced, the UCT increased. When the tool rotated around 1.8°, a very critical UCT was achieved, Fig. 6b. In this moment, a small amount of material in front of the tool tip moved upward along the edge radius, the other fraction of the workpiece was compressed beneath the tool edge and slid to the tool flank face. This critical UCT, which was defined as MCT in most cases, was important in microcutting operation. After this transition point, the shearing effect appeared between the tool and workpiece. In this simulation, the MCT was about 0.268 μm examined by FEM. It coincided with the calculation results of Wang et al. [27].

With the continuous steps, the tool advanced gradually, as shown in Fig. 6c, d. After the transition of MCT, shearing gradually became more significant than the ploughing effect, which induced the chip growth. In Fig. 6c, the workpiece material was piled up in front of the tool edge. The chip velocity vectors showed

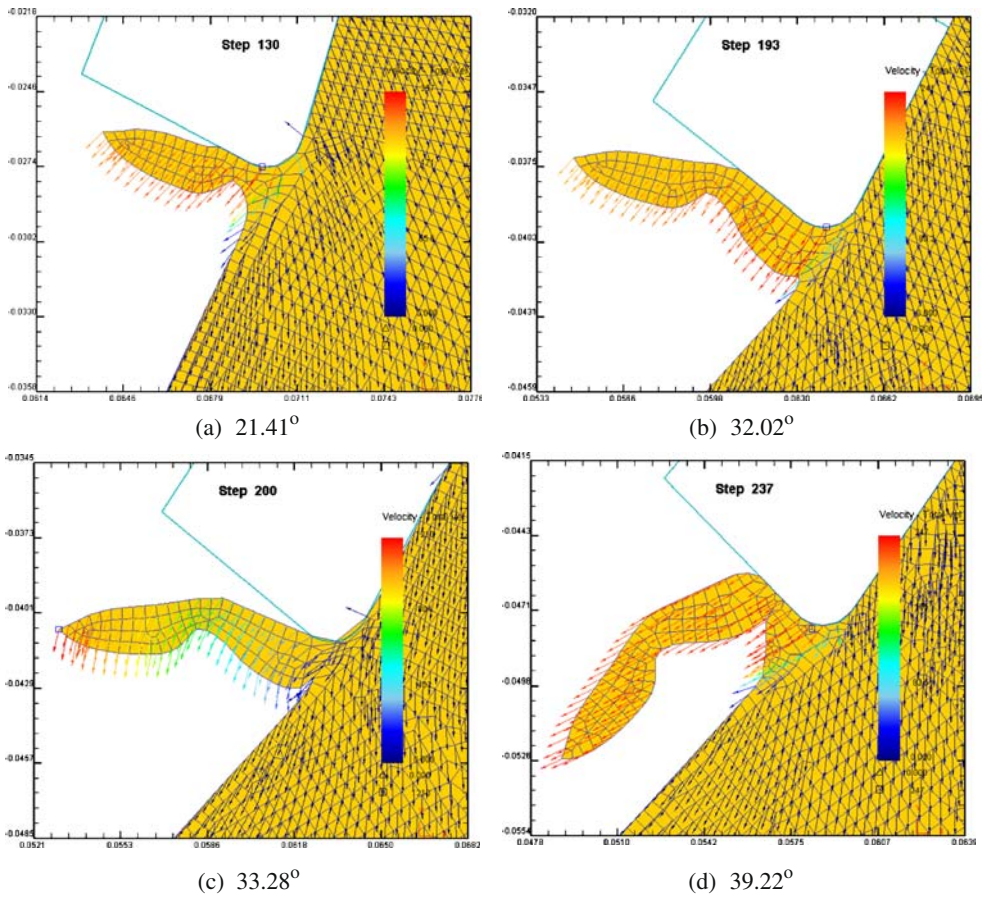

(a) 21.41° (b) 32.02°

(c) 33.28° (d) 39.22°

Fig. 7 The second segment formation process (**a**–**d**)

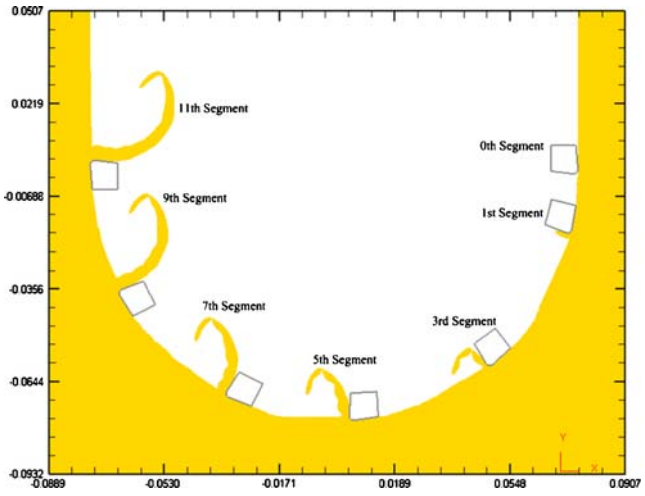

Fig. 8 The entire chip formation process

an upward trend, which represented chip growth, indicating a possible extruded-like behavior. This effect was similar to the indention operation, with a rigid ball pressing on the material. With the gradual chip growth, the velocity of the deformed material ahead of the tool tip directed almost parallel to the tool tangential movement direction, Fig. 6d. The chip was formed and the shearing effect became dominant to the chip formation process hereafter. With the chip growth, both the tool chip contact length l_T and the shear band length l_S increased continuously. More kinetic energy transferred into the chip from the tool tip. In Fig. 6e, the chip started to separate from the rake face and bent forward and downward to the uncut workpiece surface. This angular motion caused the maximal chip velocity location transferred from the chip root in the previous steps to the chip tip in this step. Then, the chip accelerated to bend, which caused the l_T to reduce and concentrate on a small section between the chip root and tool edge, as well as shortening l_S, Fig. 6f. A large portion of the kinetic energy was transferred to the chip root by the edge radius, which led the chip starting to move upward. Meanwhile, the maximal chip velocity location changed to the chip root again. Now, the first segment was formed completely, and the second segment formation process began.

As the tool advances, the tool edge continuously indented the material and the extruding phenomenon occurred again. The newly deformed materials moved forward and upward, and they impelled the first segment moving with them. With the increase of the l_T and l_S, Fig. 7a, b, the maximal chip velocity was located on the chip root. Until both l_T and l_S reached their local maximal value, the chip bending phenomenon took place once again, as shown in Fig. 7c. The maximal chip velocity was located on the chip tip in this occasion because of the additional chip angular acceleration. The second segment was produced until l_T and l_S decreased to their local minimal value and the maximal chip velocity location transferred to the chip root again, Fig. 7d.

The next few segment formation procedures were similar to the first two. However, due to the increase of the chip mass and the moment of inertia, the milling process entered the steady status gradually. In the next few segment generation occasions, although the chip maximal velocity location also varied and the chip bending motion occurred, they were not as obvious as before. The wavy chip formation in the entire micromilling process was shown in Fig. 8.

5 Chip moments calculation

5.1 Modeling of the chip formation

In this work, the chip was modeled as a cantilever to explain the chip formation process, as shown in Fig. 9. Two moments about the chip separating point O were inflicted on the chip. The first one was the "tool rake moment," M_{Tool}, from the tool rake to the chip. The second one was the "shear plane moment," M_{Work}, from the workpiece to the chip due to the normal stress on the shear plane. Both of them were scalars, and their directions are shown in Fig. 9. Therefore, the chip angular motion around the $\overrightarrow{OZ}$ axis was governed by Eq. 3. The chip mass was m_{Chip}. The chip moment of

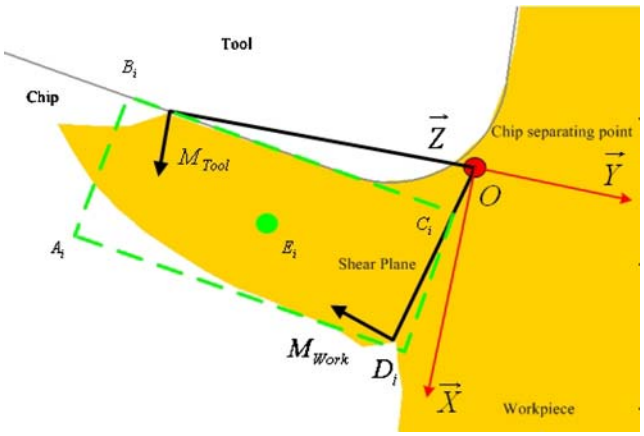

Fig. 9 Chip cantilever modeling

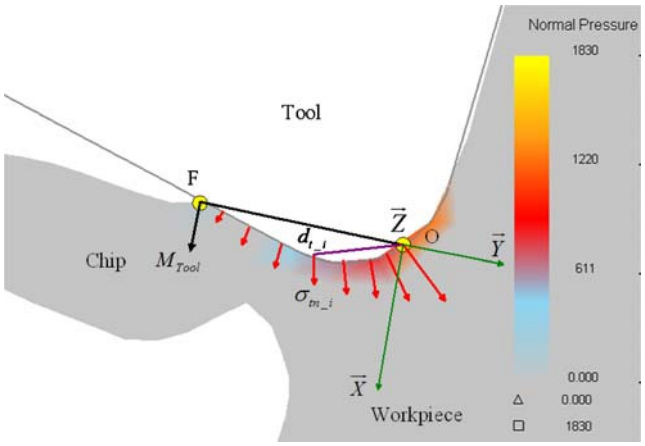

Fig. 10 M_{Tool} and tool rake normal pressure

inertia in the XY plane about $\overrightarrow{OZ}$ was $J_{\text{Chip\_O}}$. The chip angular acceleration around $\overrightarrow{OZ}$ was $\dot{\omega}_{\text{Chip}}$.

$$(M_{\text{Tool}} - M_{\text{Work}}) = J_{\text{Chip\_O}}\dot{\omega}_{\text{Chip}} \tag{3}$$

From the previous analysis, it has been found that the chip velocity varied in the chip formation process, and it could be explained if $\dot{\omega}_{\text{Chip}}$ can be obtained from the Eq. 3. Therefore, understanding the chip moments and their fluctuations was critical to clarifying the segment formation mechanism. In the subsequent sections, the hybrid FEM-analytical approach, which comprised both FEM simulation results and some analytical models, was adopted to calculate the M_{Tool} and M_{Work}.

5.2 M_{Tool} calculation

M_{Tool} was produced by the normal stress distributed on the chip-rake contact surface. It could be calculated as follows: First, the tool chip contact surface was dispersed to many infinitesimal elements from the chip separating point O, to the tool chip separating point F, Fig. 10. To each element, the normal stress value was obtained from the FEM simulation, so M_{Tool} could be calculated by Eq. 4.

$$M_{\text{Tool}} = \int_O^F w\sigma_{tn\_i}d_{t\_i}dl \tag{4}$$

σ_{tn_i} was the normal stress acting on the i_{th} element. d_{t_i} was the distance from the i_{th} element to point O. dl was the arc length of the i_{th} element. w was the chip width along the $\overrightarrow{OZ}$ axis, in this case, $w = 20$ μm.

5.3 M_{Work} calculation

M_{Work} was generated from the normal stress distribution on the shear plane, Fig. 11. Since, in the shear plane, the strain rate was significantly greater than in the other parts of the workpiece, the shear plane could be determined by the equivalent strain rate distribution plot in FEM [28]. The M_{Work} could be calculated by Eq. 5. σ_{wn_i} was the normal stress from the i_{th} element acting on the shear plane. d_{w_i} was the distance from the i_{th} element to the point O. ds is the length of the i_{th} element. The normal stress varied in a linear relationship along the shear plane, with the maximum value on point G at chip-free surface, and reduced towards the chip separating point O [29]. However, the value of σ_{wn_i} in the point O or G and the slope of σ_{wn_i} distribution were difficult to obtain till now. One of the simplifications was to assume the normal force N_S inflicted on the middle point of the shear plane [30]. In this work, this assumption was continued, and the Eq. 5 was reduced to Eq. 6, in which the average shear plane normal pressure σ_{wn_aver} was easier to calculate through dividing N_S by the shear plane area A_S, Eq. 7. A_S was calculated by Eq. 8. l_S was the shear band length. Noticing the assumption of N_S acting on the middle point of the shear plane induced some errors when calculating the M_{Work}, due to the actual acting point depending on the true distribution of σ_{wn_i}. The maximal relative error was 0.33 when σ_{wn_i} in point O was zero, but in the machining process, this value was

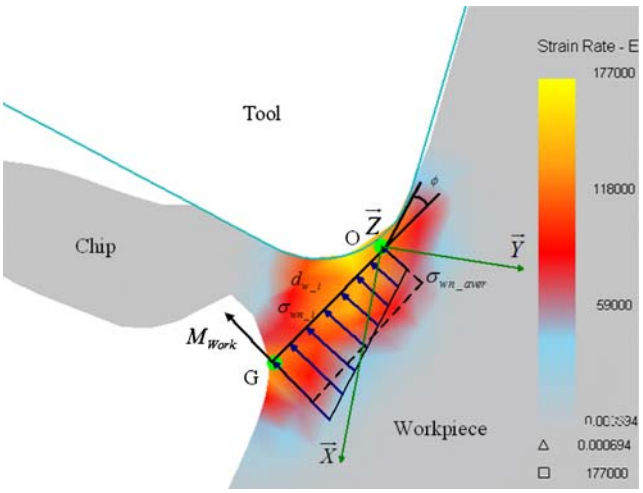

Fig. 11 M_{Work} and shear plane normal stress

always much greater than zero, so the error caused by this simplification could be very small.

$$M_{\text{Work}} = \int_O^G w\sigma_{wn\_i} d_{w\_i} ds \tag{5}$$

$$M_{\text{Work}} = \frac{w\sigma_{wn\_\text{aver}} l_s^2}{2} \tag{6}$$

$$\sigma_{wn\_\text{aver}} = \frac{N_S}{A_S} \tag{7}$$

$$A_S = w l_S \tag{8}$$

In this work, the MM model and the AD model were used to calculate the N_S, respectively, and resulted in different M_{Work}, renamed as $M_{\text{Work\_MM}}$ and $M_{\text{Work\_AD}}$. The comparison between them gave a deeper understanding of microcutting mechanism.

5.3.1 $M_{\text{Work\_MM}}$ *calculation*

In this section, N_S was calculated based on the Merchant theory [31], renamed N_{S_MM}. It assumes that the cutting forces originated from the shear work consumed in the shear plane and the friction work between the chip and tool rake. This theory is widely accepted and suitable to the conventional orthogonal cutting with greater UCT and without the consideration of the tool edge radius [30, 32].

According to the Merchant's force circle, N_{S_MM} was expressed by the cutting force F_{P_MM}, the thrust force F_{Q_MM}, and the shear angle ϕ, Eq. 9. However, only orthogonal force components F_X and F_Y could be obtained directly from the FEM simulation results. In case of orthogonal cutting hypothesis, F_{P_MM} and F_{Q_MM} in milling operation could be transformed from F_X and F_Y by the tool rotating angle θ by Eq. 10. The shear angle ϕ, defined between the tool rotating tangential direction and the shear band in the XY plane, was also obtained from FEM. The final $M_{\text{Work\_MM}}$ expression, Eq. 11, was deduced with all components from the FEM analysis.

$$N_{S\_MM} = F_{P\_MM} \sin\phi + F_{Q\_MM} \cos\phi \tag{9}$$

$$\begin{bmatrix} F_{P\_MM} \\ F_{Q\_MM} \end{bmatrix} = \begin{bmatrix} \sin\theta & \cos\theta \\ -\cos\theta & \sin\theta \end{bmatrix} \begin{bmatrix} F_X \\ F_Y \end{bmatrix} \tag{10}$$

$$M_{\text{Work\_MM}} = \frac{[-\cos(\theta+\phi)F_X + \sin(\theta+\phi)F_Y] l_s}{2} \tag{11}$$

5.3.2 $M_{\text{Work\_AD}}$ *calculation*

Because the machining parameters and tool geometric features in micromilling operation are obviously different from the conventional cutting, it has been found that the microcutting forces were produced not only by the shearing effect ahead of the tool tip, but also by the tool workpiece ploughing, friction, and workpiece springback effects. The most important reason for these effects is the reduced ratio of UCT to the cutting edge radius. The specific cutting energy increases exponentially to approximately 100-times that in the conventional scale. Arcona and Dow [21] proposed a cutting force model for diamond machining based on the elastic contact and friction between the tool and some workpiece materials, including Al6061-T6 alloy. The model also included shearing forces for a very sharp and rigid tool; the results showed that, as the UCT reduced, the shearing contribution to the total cutting forces greatly decreased while the elastic contact and friction components approached an asymptotic level. These parasitical forces were attributed to the workpiece elastic springback as it was compressed and moved under the cutting edge without being removed. The AD model required the hardness and Young's modulus of the workpiece, and two empirical constants were obtained from cutting measurements. Therefore, it was much easier to imbed into the NC system than other complex mechanic models for the online manufacturing compensation. Although it was first developed for the diamond turning force calculation purpose, the following investigators resorted to modifying and employing the AD model into the micromilling process. Dow et al. [33] integrated the AD model into the NC system to predict the cutting and thrust forces of the small ball end milling of S-7 tool steel and compensated shape error induced by the tool deflection. Friedrich et al. [20] modified the AD model to investigate the workpiece springback effect on the micromilling force components. Gong et al. [34] used the AD model to calculate the micromilling force considering the tool rotational error.

The major differences between the micromilling and diamond cutting are that the milling tool edge radii are in the order of several micrometers, the milling tool has a variable UCT for each edge, and the milling tool has multiple edges in contact with the workpiece with time-varying force resultants at any instant of tool rotation. The AD model adopted into one generalized micromill tool edge, either the side edge or the bottom edge, was illustrated in Fig. 12.

The AD model is expressed as Eq. 12. H and E are the hardness and Young's modulus of the workpiece material, respectively. A_C is the face area of

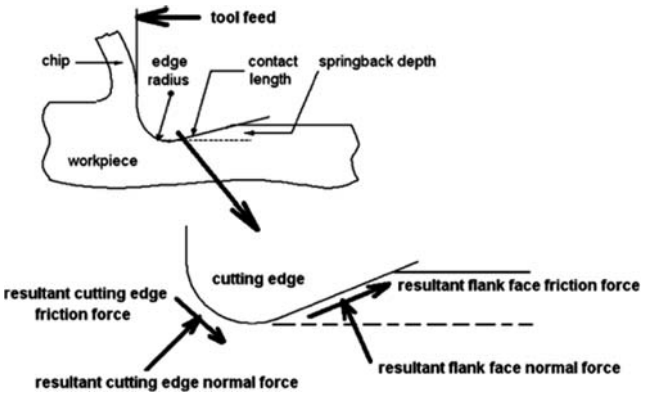

Fig. 12 Generalized micromilling tool cutting edge and flank with resultant normal contact forces and friction forces. Magnitude and orientation of resultant force vectors depend on tool geometry and work piece springback depth [20]

the chip. A_f is the tool flank contact area with the workpiece. μ is the friction coefficient between the tool rake face and workpiece. μ_f is the friction coefficient between flank face and workpiece. ϕ is the shear angle. The cutting force F_{P_AD} in Eq. 12 consists of two terms. The first one is the force on the rake face. It is a function of the workpiece material and A_C. The second term originates from the friction on the flank face of the tool, and it is a function of the workpiece material, A_f and μ_f. The thrust force F_{Q_AD} in Eq. 12 is similar to the cutting force, with the first term originating from friction on the rake face and the second from the direct force on the flank face. The constants in Eq. 12 were experimentally obtained as a best fit for several materials including Al6061-T6 [21]. In this model, it is obvious that the second term of each force component is the contribution of the workpiece springback on the flank face. The first term is related to the shearing effect on the rake face.

In order to calculate the cutting force only due to the effects from tool rake, each second item in Eq. 12 was ignored, and the final expressions of F_{P_AD} and F_{Q_AD} were reduced to Eq. 13. Integrating them into the normal force on the shear plane N_{S_AD}, Eq. 14, and input N_{S_AD} into Eq. 7, the $M_{\text{Work\_AD}}$ was given in Eq. 15.

$$\begin{cases} F_{P\_AD} = \frac{HA_C}{3}\left(\frac{\cot\phi}{\sqrt{3}}+1\right) + \mu_f A_f\left[(4.1H)\sqrt{\frac{H}{E}}\right] \\ F_{Q\_AD} = \mu\left[\frac{HA_C}{3}\left(\frac{\cot\phi}{\sqrt{3}}+1\right)\right] + A_f\left[(4.1H)\sqrt{\frac{H}{E}}\right] \end{cases} \tag{12}$$

$$\begin{cases} F_{P\_AD} = \frac{HA_C}{3}\left(\frac{\cot\phi}{\sqrt{3}}+1\right) \\ F_{Q\_AD} = \mu\left[\frac{HA_C}{3}\left(\frac{\cot\phi}{\sqrt{3}}+1\right)\right] \end{cases} \tag{13}$$

$$N_{S\_AD} = F_{P\_AD}\sin\phi + F_{Q\_AD}\cos\phi \tag{14}$$

$$M_{\text{Work\_AD}} = \frac{wl_s^2 H\sin\phi}{6}\left(\frac{\cot\phi}{\sqrt{3}}+1\right)(\sin\phi+\mu\cos\phi) \tag{15}$$

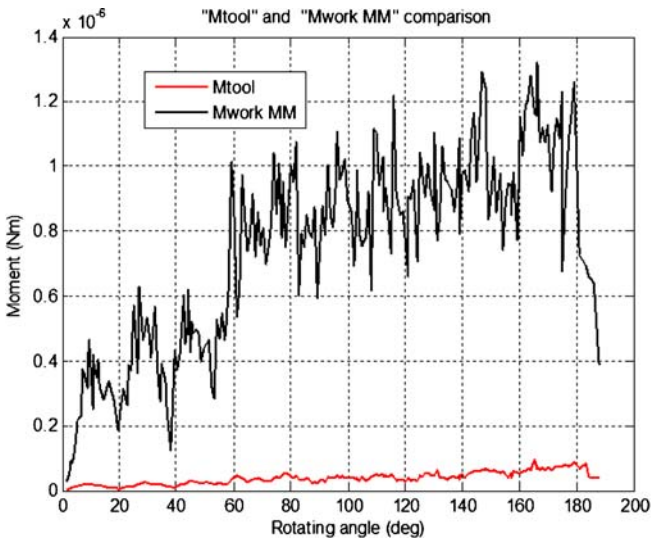

(a) M_{Tool} and M_{Work_MM}

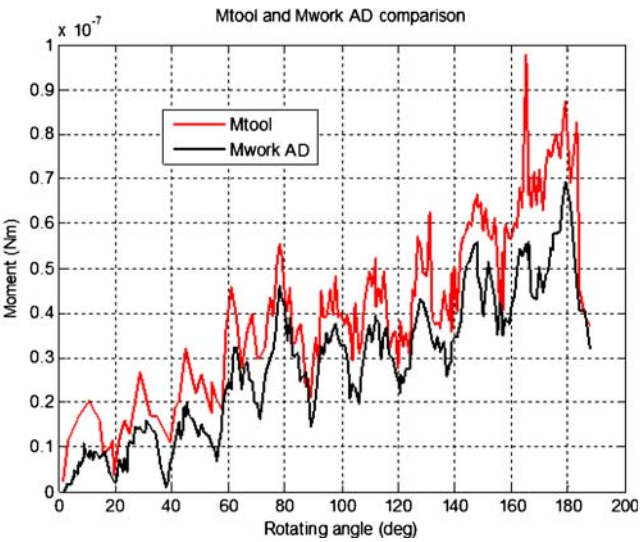

(b) M_{Tool} and M_{Work_AD}

Fig. 13 M_{Tool} vs $M_{\text{Work\_MM}}$ and M_{Tool} vs $M_{\text{Work\_AD}}$ (**a**, **b**)

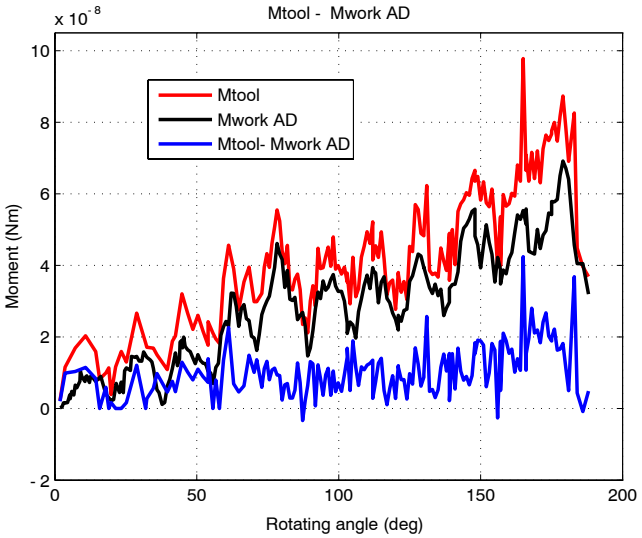

Fig. 14 M_{Tool}, $M_{\text{Work\_AD}}$ and $M_{\text{Tool}} - M_{\text{Work\_AD}}$ variations

6 Chip moment calculation results

In this section, the calculation results of the M_{Tool} and M_{Work} ($M_{\text{Work\_MM}}$ and $M_{\text{Work\_AD}}$) are given in detail. Figure 13 gives the comparisons between M_{Tool} and $M_{\text{Work\_MM}}$ and between M_{Tool} and $M_{\text{Work\_AD}}$.

In Fig. 13a, it was obvious that $M_{\text{Work\_MM}}$ was much greater than M_{Tool}. Should this be true, the chip would not form the wavy segment and grow up. This was contradictory with the simulation results and the experimental observation.

In Fig. 13b, M_{Tool} was a little greater than $M_{\text{Work\_AD}}$, with similar variation curves. When the chip segment started to form, both of them were in the local minimum values and reached the local maximum values when it started to bend. With the decrease of l_T and l_S, both of them reduced to other local minimum values. The curves had 11 waves, which corresponded to the 11 segments. From Eq. 3, it was seen that the difference of M_{Tool} and $M_{\text{Work\_AD}}$, $M_{\text{Tool}} - M_{\text{Work\_AD}}$, induced the chip angular motion and segment generation. These three variables are given in Fig. 14. Although the difference $M_{\text{Tool}} - M_{\text{Work\_AD}}$ fluctuated, its deviation was small, and it did not increase as the chip moments. When the M_{Tool} and $M_{\text{Work\_AD}}$ reached their local maximal values, the chip started to bend in this instant. Some peak values existed to induce the additional chip angular acceleration. This procedure repeated for each segment generations in the entire micromilling process and coincided with the FEM simulation and experimental results.

The comparison of the chip moment calculation results also indicated that the widely accepted MM model was not valid in the microcutting. Additional works were required to develop new models adapted to the microcutting, and the AD model could be a good candidate.

Therefore, it was important to clarify the main reasons of the M_{Tool} and $M_{\text{Work\_AD}}$ variations, which were the primary reasons for the wavy chip formation. In the chip moments calculation, the chip width w was a constant. So in Eq. 6, the $M_{\text{Work\_AD}}$ was a function of the shear band length l_S and the average shear plane

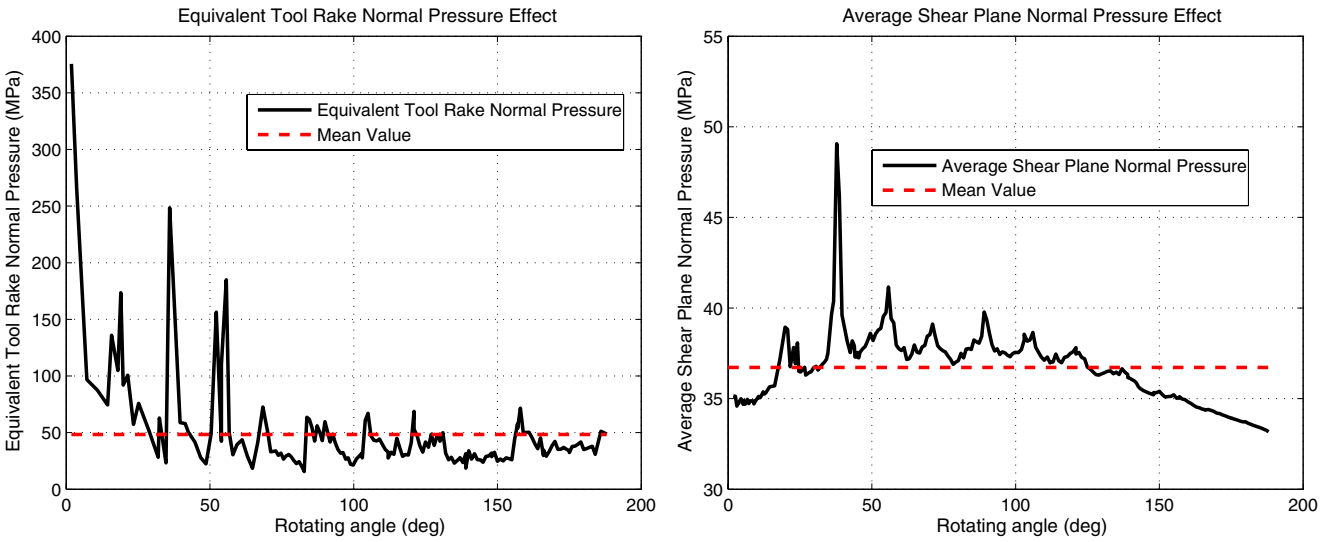

(a) σ_{tn_equ} (b) $\sigma_{\omega n\_aver}$

Fig. 15 σ_{tn_equ} and σ_{wn_aver} variations (**a**, **b**)

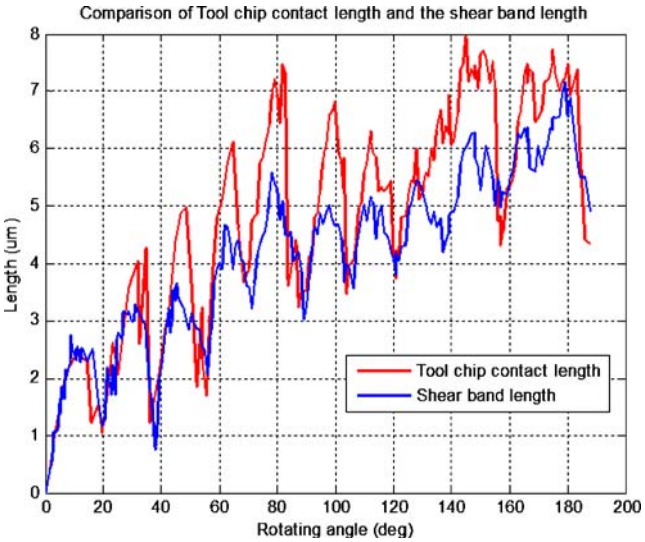

Fig. 16 The variation of the tool chip contact length l_T and the shear band length l_S

normal pressure σ_{wn_aver}, $M_{\text{Work\_AD}} = f(l_S^2/2, \sigma_{wn\_aver})$. In Eq. 15, the σ_{wn_aver} was caused by the shear angle ϕ. Similar to $M_{\text{Work\_AD}}$, the M_{Tool} was simplified in Eq. 4 as a function of the tool chip contact length l_T and the equivalent tool rake normal stress σ_{tn_equ}, $M_{\text{Tool}} = f(l_T^2/2, \sigma_{tn\_equ})$.

Figure 15 gave variations of σ_{tn_equ} and σ_{wn_aver} in the entire milling process. Obviously, they did not follow the same trends as the M_{Tool} and $M_{\text{Work\_AD}}$. Additionally, their magnitudes were not great, although there were some exceptions, as follows: At the beginning of the tool workpiece engagement, the σ_{tn_equ} value was much greater. This was the so-called size effect due to the extra-small UCT. Then, in the first three segment generation occasions, there were some greater values because the shorter l_T induced the increase of the specific cutting energy. Especially when the second segment occurred, after the tool rotated about 40°, because the l_T and l_S were the shortest in this occasion, as shown in Fig. 16, both σ_{tn_equ} and σ_{wn_aver} were higher due to the higher specific cutting energy. From Fig. 16, it was obviously that l_T and l_S fluctuated in trends similar to M_{Tool} and $M_{\text{Work\_AD}}$. Before the chip bending, l_T and l_S accompanied with the M_{Tool} and $M_{\text{Work\_AD}}$ increased simultaneously. According to the works of Childs [29] and Astakhov [35], the normal stress distributed on the shear plane had an upper limit. When $M_{\text{Work\_AD}}$ reached its local maximal value, l_S achieved its local maximal value too. Due to the continuous tool advancing, M_{Tool} still increased with l_T. Then, the difference of $M_{\text{Tool}} - M_{\text{Work\_AD}}$ increased enough to make the chip get the additional angular acceleration and bend. The M_{Tool} and l_T achieved their local maximal values when the chip began to bend. After the chip separated from the tool rake in the chip bending process, the l_T decreased faster and induced the decreases of other variables, such as M_{Tool}, $M_{\text{Work\_AD}}$, and l_S. In Fig. 16, the l_T decreased faster than the l_S in the chip bending process, so the decrease of l_T induced the chip bending. After the chip bending angular motion finished, all of these variables achieved

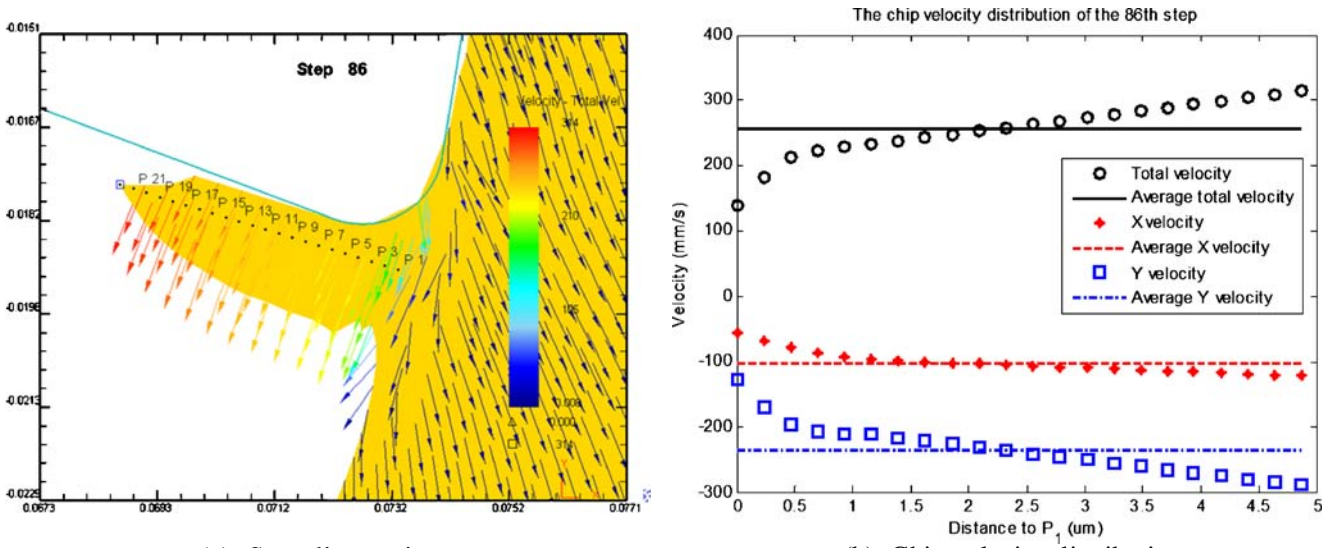

(a) Sampling points (b) Chip velocity distribution

Fig. 17 Chip velocity distribution before the first segment separating with tool(**a**, **b**)

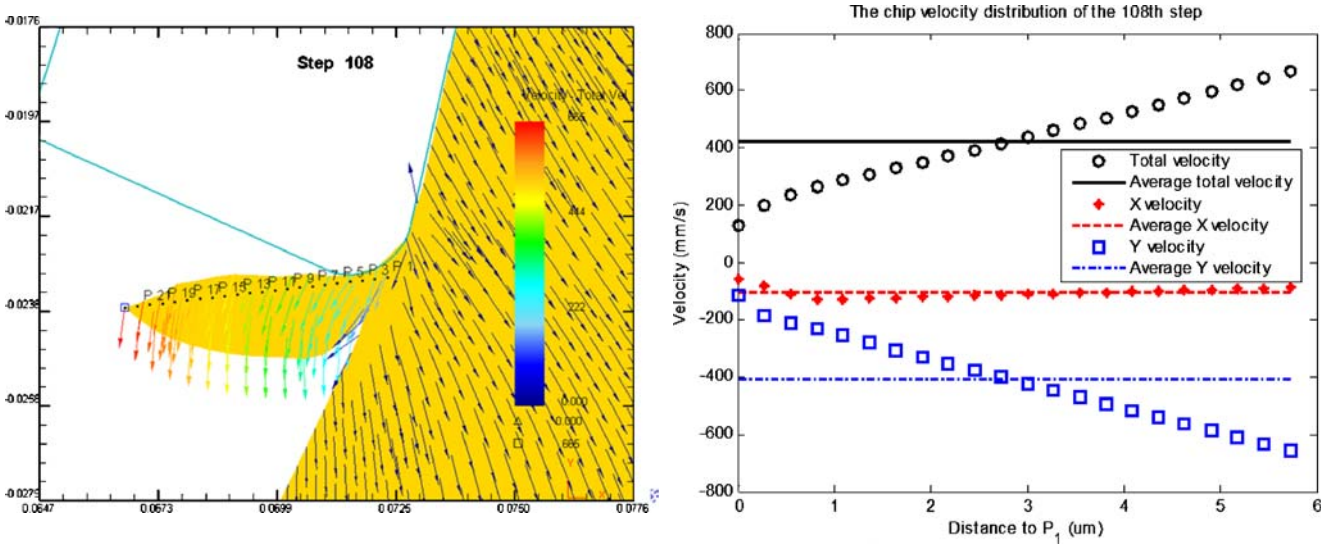

(a) Sampling points (b) Chip velocity distribution

Fig. 18 Chip velocity distribution after the first segment separating with tool (**a**, **b**)

their local minimal values, the chip started to grow again, and the segment was formed. This procedure repeated and repeated for each segment generation. Due to the smaller chip mass and moment of inertia, these phenomena were obvious, especially in the first few segment generation processes. Therefore, the l_S and l_T induced the M_{Tool} and $M_{\text{Work\_AD}}$ fluctuating with the same trend as them. Therefore, the main reasons of the segment chip were the variations of l_S and l_T.

7 Chip velocity analysis

From the analysis of chip formation processes, the maximal chip velocity changed from the chip root to the chip tip, then back to the chip root in each segment generation. This phenomenon was obvious when the chip mass and moment of inertia were smaller.

Figures 17 and 18 gave the comparison of chip velocity distribution before and after the chip separated

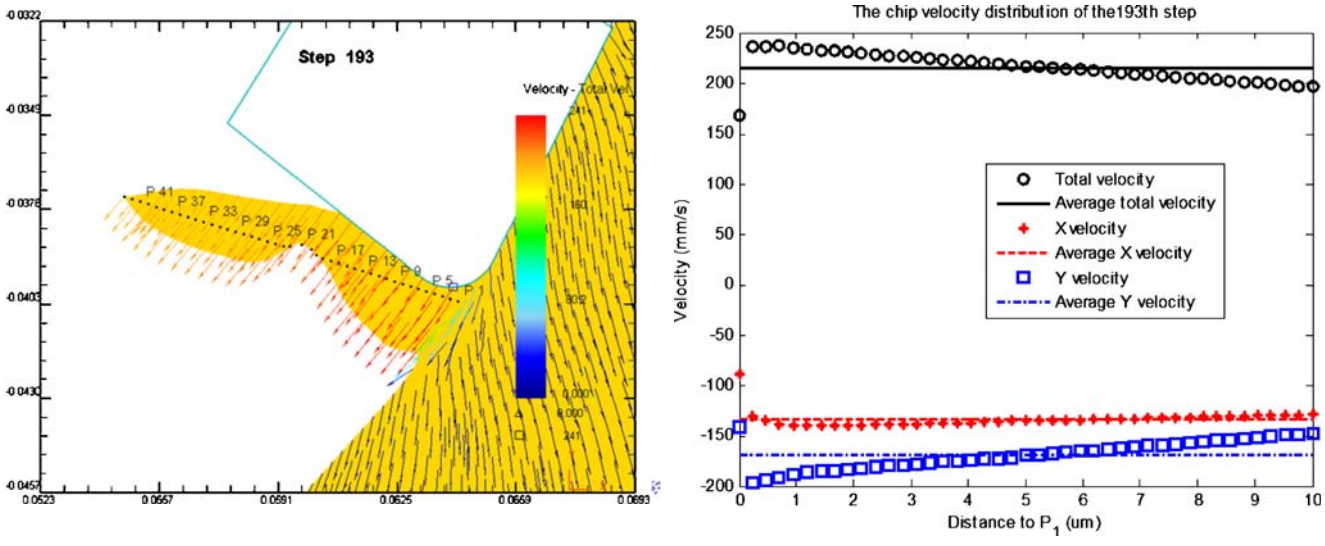

(a) Sampling points (b) Chip velocity distribution

Fig. 19 Chip velocity distribution before the second segment separating with tool (**a**, **b**)

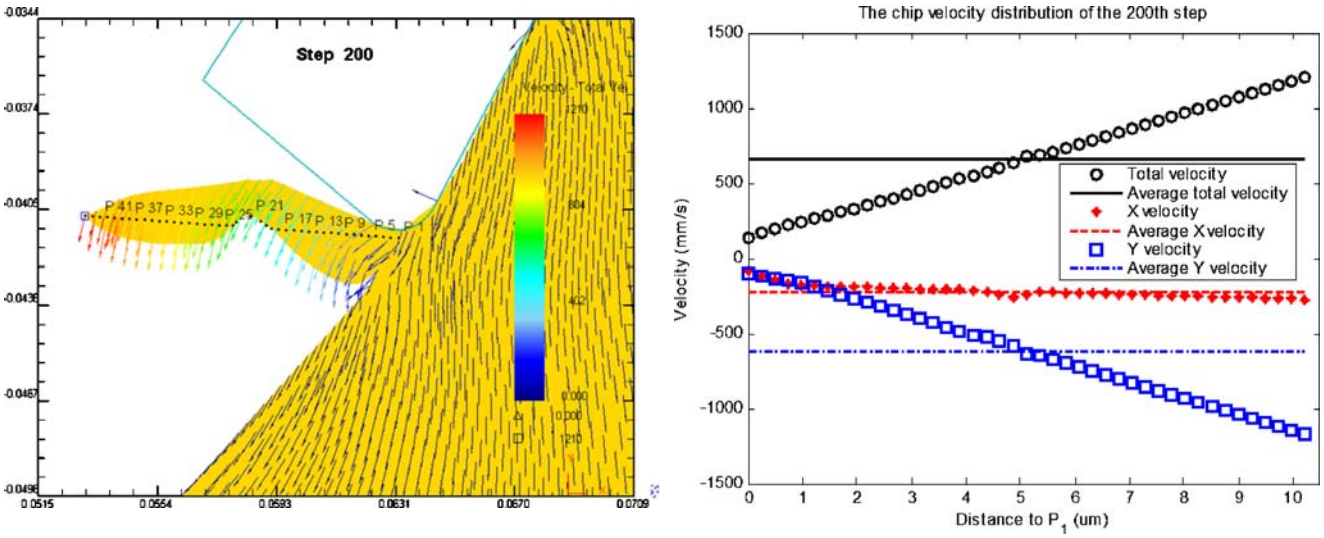

(a) Sampling points (b) Chip velocity distribution

Fig. 20 Chip velocity distribution after the second segment separating with tool (**a**, **b**)

with the tool at the first segment generation instant. The average velocity value in Fig. 18 was 424.6 mm/s, but in Fig. 17, this value was only 256.2 mm/s, which was similar to the cutting speed, 238.8 mm/s. The chip velocity ranged from 138.8 to 314.4 mm/s in Fig. 17 and from 130.8 to 665.3 mm/s in Fig. 18, respectively.

Similar to Figs. 17 and 18, Figs. 19 and 20 represent the chip velocity distribution when the second segment formed. Similar results were found with the comparison between Figs. 17 and 18. The average velocity value was 662.9 mm/s in Fig. 20, much higher than the corresponding value in Fig. 19, 215.7 mm/s, which was also close to the cutting speed. The chip velocity ranged from 167.5 to 235.8 mm/s in Fig. 19 and from 133.8 to 1,206 mm/s in Fig. 20.

From the analysis in this section, it has been found that the average chip velocity magnitudes after the chip separating from the tool (Figs. 18 and 20) were much greater than those before the chip bending, (Figs. 17 and 19), which were about the nominal cutting speed. Meanwhile, the velocity in the shear plane was almost constant for all cases, but during the chip bending process, the chip tip velocities in Figs. 18 and 20 were greater because of the chip angular acceleration, as calculated in the next section.

8 Chip angular acceleration analysis

After acquiring the chip velocity distribution in the adjoining steps from FEM, the chip angular acceleration obtained from FEM analysis $\dot{\omega}_{\text{Chip\_FEM}}$ could be calculated as follows:

$$\dot{\omega}_{\text{Chip\_FEM}} = \frac{\frac{V_{\text{tip\_}e} - V_{\text{root\_}e}}{D_e} - \frac{V_{\text{tip\_}b} - V_{\text{root\_}b}}{D_b}}{T_e - T_b} \tag{16}$$

In Eq. 16, $V_{\text{tip\_}b}$ was the chip tip velocity in the beginning step. $V_{\text{tip\_}e}$ was the chip tip velocity in the end step. $V_{\text{root\_}b}$ was the chip root velocity in the beginning step. $V_{\text{root\_}e}$ was the chip root velocity in the end step. D_b was the distance from chip root to chip tip in the beginning step. D_e was the distance from chip root

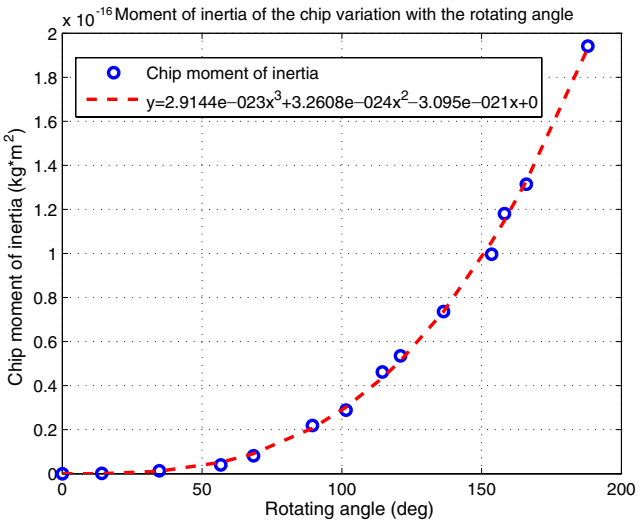

Fig. 21 The moment of inertia of the chip variation with the rotating angle

to chip tip in the end step. T_b was the time of the beginning step. T_e was the time of the end step. All of these elements could be obtained from FEM results, and for the first and second segments, they were shown in Figs. 17–20.

Meanwhile, M_{Tool} and $M_{\text{Work\_AD}}$ could be calculated in Section 6. If the chip moment of inertia $J_{\text{Chip\_O}}$ was obtained, Eq. 3 could be used to calculate $\dot{\omega}_{\text{Chip}}$ in another way. Then, the comparison between $\dot{\omega}_{\text{Chip}}$ and $\dot{\omega}_{\text{Chip\_FEM}}$ could be utilized to validate the correctness of M_{Tool} and $M_{\text{Work\_AD}}$ calculations. As shown in Fig. 9, the chip was modeled as a cantilever with a series segment. Hence, $J_{\text{Chip\_O}}$ could be calculated approximately as follows: First, it is assumed that the chip was homogeneous, without the density variation in the cutting process. The i^{th} chip segment was simplified as a rectangular shape $A_iB_iC_iD_i$, with length l_i, width b_i, and geometric shape center E_i. The subscript i represented the segment sequence number, from 1 to n, here $n = 11$. For the i_{th} segment, its moment of inertia about the $\overrightarrow{OZ}$ axis across its own geometric shape center E_i was J_{E_i}, which was calculated by Eq. 17. According to the "parallel axis theorem," to the entire formed chip, $J_{\text{Chip\_O}}$ was expressed by Eq. 18, in which d_i was the distance from E_i to the point O, and m_i was the mass of the i_{th} segment, which was the product of the workpiece density ρ and the volume of the chip, estimated by Eq. 19.

$$J_{E_i} = \frac{m_i(l_i^2 + b_i^2)}{12} \tag{17}$$

$$J_{\text{Chip\_O}} = \sum_{i=1}^{n}(J_{E_i} + m_i d_i^2) \tag{18}$$

$$m_i = \rho l_i b_i w \tag{19}$$

When each segment formed, $J_{\text{Chip\_O}}$ was calculated at the corresponding rotating angle. Due to chip curling, $J_{\text{Chip\_O}}$ increased in a nonlinear trend. At the beginning of the micromilling, $J_{\text{Chip\_O}}$ was smaller. This was the reason why the chip acquires great velocity in the first few segment formation processes. By polynomial curve fitting, $J_{\text{Chip\_O}}$ was found to be a third-order function with reference to the rotating angle in the entire process, Fig. 21. Due to the fact that $J_{\text{Chip\_O}} = 0$ when the rotating angle was 0°, the fitting function utilized $J_{\text{Chip\_O}}/\theta$ vs θ instead of $J_{\text{Chip\_O}}$ vs θ. Therefore, the coefficient for the zero-order item in this function shown in Fig. 21 was set to zero, and its final expression was Eq. 20.

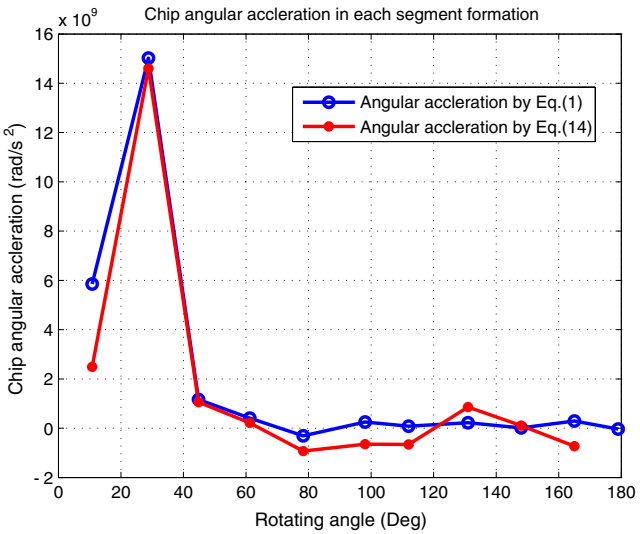

Fig. 22 The chip angular acceleration comparison between $\dot{\omega}_{\text{Chip\_FEM}}$ and $\dot{\omega}_{\text{Chip}}$

$$J_{\text{Chip\_O}} = 2.9144e^{-23}\theta^3 + 3.2608e^{-24}\theta^2 - 3.095e^{-21}\theta \tag{20}$$

The comparison between $\dot{\omega}_{\text{Chip\_FEM}}$ calculated by Eq. 16 and $\dot{\omega}_{\text{Chip}}$ calculated by Eq. 3 is shown in Fig. 22. Two calculation results matched well within a small error range. Hence, the calculations of M_{Tool} and $M_{\text{Work\_AD}}$ were validated.

9 Conclusions

In this work, the chip formation in the slot micromilling process by one flute cutter was investigated by FEM and experimentation. Based on the suitable assumptions, the micromilling operation was modeled in DEFORM-2D. The JC constitutive and Coulomb's friction models were adopted in the FEM simulation. The segmented chip was found when micromilling Al6061-T6 by carbide tool under this machining parameter set. The simulated chip morphology, segment length, and cutting force matched the experimental results with acceptable error. Through analyzing the chip velocity, the chip formation process was described in detail. The chip formation mechanism was studied quantitatively via a hybrid FEM–analytical approach. Some important results were found, as follows:

1. The fluctuations of the tool chip contact length l_T and the shear band length l_S were the main reasons

for segment formation. They induced the variations of the M_{Work} and M_{Tool}.

2. The variation of difference between M_{Tool} and M_{Work}, $M_{\text{Tool}} - M_{\text{Work}}$, caused the additional chip angular acceleration and induced the chip velocity increase when the segment formed.
3. The maximal chip velocity located in the chip root before and after segment generation. In the wavy segment-forming instant, the maximal chip velocity location changed to the chip tip because the chip got additional angular acceleration caused by an increase of the chip moment difference.
4. The MM and AD models were used to calculate M_{Work}. The comparison between their results showed the MM model was not suitable in the microcutting scale, although it was widely accepted in the conventional scale. The AD model could be a good candidate in this field.
5. When the wavy segment occurred, the average chip velocity magnitude was much greater than the one before the segment generation, which was about the cutting speed. The chip root velocity was almost constant in the entire micromilling process, and the chip tip velocity increased greatly when the chip bent.
6. When the chip segment formed, it acquired additional angular acceleration and induced the increase of chip velocity. The chip angular acceleration was obtained, respectively, by FEM and analytical model based on the M_{Tool} and $M_{\text{Work\_AD}}$ calculation results. The agreement of these two approaches validated the calculations of M_{Tool} and $M_{\text{Work\_AD}}$.

This work gave a deep understanding of the segmented chip formation mechanism in micromilling operation. The revealed mechanism can be used to explain the chip formation mechanism when micromilling other materials because of the inherence of smaller chip mass and moment of inertia in the micromilling process.

In the future, the complex microtool rotational error will be integrated into the FEM analysis and the tool edge radius effect will be studied quantitatively. The polycrystalline material with anisotropic metal phase properties will be embedded into the simulation engine, and the crystal plasticity constitutive model will be adopted to explain the microcutting mechanism on the polycrystalline metals.

Acknowledgements The authors appreciate the kindly help from colleagues in LAMA of NEU and LGIPM of UPV. Greatest acknowledgement goes to Prof. Kai Cheng from Brunel University for his suggestions on paper revising and to Dr. Tugrul Özel from Rutgers University for his english proof-reading.

References

1. Dornfeld D, Min S, Takeuchi Y (2006) Recent advances in mechanical micromachining. Ann CIRP 55(2):745–768
2. Alting L, Kimura F, Hansen H, Bissacco G (2003) Micro engineering. Ann CIRP 52(2): STC–O
3. Weule H, Huntrup V, Tritschler H (2001) Micro-cutting of steel to meet new requirements in miniaturization. Ann CIRP 50:61–64
4. Bang Y, Lee K, Oh S (2005) 5-axis micro milling machine for machining micro parts. Int J Adv Manuf Technol 25:888–894
5. Wang J, Gong Y, Abba G, Cao J, Shi J, Cai G (2007) Micro milling technologies for mems. In: Proceeding of 3rd MEMSTECH, Lviv-Polyana, 23–26 May 2007, pp 86–95
6. Astakhov V, Shvets S, Osman M (1997) Chip structure classification based on mechanics of its formation. J Mater Process Technol 71(2):247–257
7. Ueda K, Manabe K (1992) Chip formation mechanism in microcutting of an amorphous metal. Ann CIRP 41(1):129–132
8. Lee K, Dornfeld D (2002) An experimental study on burr formation in micro milling aluminium and copper. Trans North Am Manuf Res Inst SME 30:255–262
9. Usui E, Shirakashi T (1982) Mechanics of machining from descriptive to predictive theory, on the art of cutting metals. ASME PED 7:13–35
10. Özel T, Altan T (2000) Process simulation using finite element method—prediction of cutting forces, tool stresses and temperatures in high-speed flat end milling. Int J Mach Tools Manuf 40(5):713–738
11. Özel T, Zeren E (2007) Finite element modeling the influence of edge roundness on the stress and temperature fields induced by high-speed machining. Int J Adv Manuf Technol 35:255–267
12. Vogler M, DeVor R, Kapoor S (2004) On the modeling and analysis of machining performance in micro-endmilling, part I: surface generation. ASME J Manuf Sci Eng 126:684–693
13. Chuzhoy L, DeVor R, Kapoor S, Beaudoin A, Bammann D (2003) Machining simulation of ductile iron and its constituents. Part I: estimation of material model parameters and their validation. ASME J Manuf Sci Eng 125:181–191
14. Simoneau A, Ng E, Elbestawi M (2006) Chip formation during microscale cutting of a medium carbon steel. Int J Mach Tools Manuf 46:467–481
15. Dhanorker A, Özel T (2008) Meso/micro scale milling for micro-manufacturing. Int J Mechatron Manuf Syst 1:23–42
16. Woon K, Rahman M, Fang F, Neo K, Liu K (2008) Investigations of tool edge radius effect in micromachining: a fem simulation approach. J Mater Process Technol 195:204–211
17. Cheng K, Luo X, Ward R, Holt R (2003) Modeling and simulation of the tool wear in nanometric cutting. Wear 255(7–12):1427–1432
18. Shi J, Liu C (2004) The influence of material models on finite element simulation of machining. ASME J Manuf Sci Eng 126(4):849–857
19. Özel T (2006) The influence of friction models on finite element simulations of machining. Int J Mach Tools Manuf 46(5):518–530
20. Friedrich C, Kulkarni V (2004) Effect of workpiece springback on micromilling forces. Microsyst Technol 10:472–477

21. Arcona C, Dow T (1998) An empirical tool force model for precision machining. ASME J Manuf Sci Eng 120:700–707.
22. Johnson G, Stryk R, Holmquist T, Beissel S (1996) User instruction for the 1996 version of the epic code. Tech. Rep., Alliant Techsystems Inc
23. Özel T, Zeren E (2004) Determination of work material flow stress and friction properties for fea of machining using orthogonal cutting tests. J Mater Process Technol 153–154:1019–1025
24. Trent E, Wright P (2000) Metal cutting, 4th edn. Butterworth-Heinemann, Woburn
25. Medaska M, Nowag L, Liang S (1999) Simultaneous measurement of the thermal and mechanical effectiveness of cutting fluid. J Mach Sci Technol 3(2):221–237
26. Shaw M (1993) Chip formation in the machining of hardened steel. Ann CIRP 42(1):29–33
27. Wang J, Gong Y, Abba G, Chen K, Shi J, Cai G (2008) Surface generation analysis in micro end-milling considering the influences of grain. Microsyst Technol 14(7):937–942
28. Bil H, Kiliç S, Tekkaya A (2004) A comparison of orthogonal cutting data from experiments with three different finite element models. Int J Mach Tools Manuf 44(2):933–944
29. Childs T, Maekawa K, Obikawa T, Yamane Y (2000) Metal machining: theory and applications. Arnold, London
30. Moufki A, Molinari A, Dudzinski D (1998) Modelling of orthogonal cutting with a temperature dependent friction law. J Mech Phys Solids 35(9):1092–1027
31. Merchant M (1945) Mechanics of the metal cutting process 1: orthogonal cutting and a type 2 chip. J Appl Physi 16(5):267–275
32. Venuinod P, Jin W (1996) Three-dimensional cutting force analysis based on the lower boundary of the shear zone. Part 1: single edge oblique cutting. Int J Mach Tools Manuf 36(3):307–323
33. Dow T, Miller E, Garrard K (2004) Tool force and deflection compensation for small milling tools. Precis Eng 28: 31–45
34. Gong Y, Wang J, Abba G, Antoine J, Shi J (2008) Tool tip trajectories investigation and its influences in micromilling operation. In: 3rd IEEE International Conference on Nano/Micro Engineered and Molecular Systems, Sanya, 6–9 January 2008, pp 440–445
35. Astakhov V (1998) Metal cutting mechanics. CRC, Boca Raton